Development of Finite Element Formulations for High-Fidelity Polycrystals and Damage Avoidance in Friction Stir Welding
Grant N00014-06-1-0241 Final Report Technical Section

Paul Dawson, PI
Sibley School of Mechanical and Aerospace Engineering
Cornell University

Abstract

This report provides the technical summary and a few representative results of the research conducted at Cornell University under the support from the Office of Naval Research under Grant N00014-06-1-0241. Topic-by-topic citations to refereed journal publications resulting from the research are provided.

20100730235

REPORT DOCUMENTATION PAGE

Form Approved
OMB No. 0704-0188

The public reporting burden for this collection of information is estimated to average 1 hour per response, including the time for reviewing instructions, searching existing data sources, gathering and maintaining the data needed, and completing and reviewing the collection of information. Send comments regarding this burden estimate or any other aspect of this collection of information, including suggestions for reducing the burden, to Department of Defense, Washington Headquarters Services, Directorate for Information Operations and Reports (0704-0188), 1215 Jefferson Davis Highway, Suite 1204, Arlington, VA 22202-4302. Respondents should be aware that notwithstanding any other provision of law, no person shall be subject to any penalty for failing to comply with a collection of information if it does not display a currently valid OMB control number.
PLEASE DO NOT RETURN YOUR FORM TO THE ABOVE ADDRESS.

1. REPORT DATE *(DD-MM-YYYY)*	2. REPORT TYPE	3. DATES COVERED *(From - To)*
July 26, 2010	Final Technical	Jan 2006 Dec 2008

4. TITLE AND SUBTITLE
Development of finite element formulations for high fidelity polycrystals and damage avoidance in friction stir welding

5a. CONTRACT NUMBER

5b. GRANT NUMBER
N00014-06-1-0241

5c. PROGRAM ELEMENT NUMBER

5d. PROJECT NUMBER

5e. TASK NUMBER

5f. WORK UNIT NUMBER

6. AUTHOR(S)
Dawson, Paul R.

7. PERFORMING ORGANIZATION NAME(S) AND ADDRESS(ES)
Cornell University
Office of Sponsored Programs
373 Pine Tree Road
Ithaca, NY 14850-2820

8. PERFORMING ORGANIZATION REPORT NUMBER
NONE

9. SPONSORING/MONITORING AGENCY NAME(S) AND ADDRESS(ES)
Office of Naval Research
875 North Randolph Street
Arlington, VA 22203-1995

10. SPONSOR/MONITOR'S ACRONYM(S)
ONR

11. SPONSOR/MONITOR'S REPORT NUMBER(S)
NONE

12. DISTRIBUTION/AVAILABILITY STATEMENT
Approved for public release, distrbution is unlimited.

13. SUPPLEMENTARY NOTES
NONE

14. ABSTRACT
The research funded under this grant had two primary objectives. The first objective focused on advancing the technology of friction stir welding (FSW) in shipbuilding. We developed finite element based simulation methods that can help identify those conditions conducive to defect development in the welded joint. Our objective was to identify processing windows that avoid conditions that promote macroscopic defects called ``wormholes." The second objective focused on advancing micromechanical models for plastic deformation of structural alloys used in ship building. We are addressing two aspects of the mechanical behavior: the stress distribution as the metal yields under different states of stress and the yield asymmetry that develops between tension and compression following plastic deformation. As part of this objective, we developed neutron diffraction experiments with in situ biaxial loading that permit us to better motivate and critique the micromechanical models.

15. SUBJECT TERMS
Friction stir welding, damage, finite element modeling, crystal plasticity, neutron diffraction.

16. SECURITY CLASSIFICATION OF:			17. LIMITATION OF ABSTRACT	18. NUMBER OF PAGES	19a. NAME OF RESPONSIBLE PERSON
a. REPORT	b. ABSTRACT	c. THIS PAGE			Tammy Custer
U	U	U	UU	18	19b. TELEPHONE NUMBER *(Include area code)* 607-255-5014

Standard Form 298 (Rev. 8/98)
Prescribed by ANSI Std. Z39.18

1 Introduction

The research funded under this grant had two primary objectives. The first objective focused on advancing the technology of friction stir welding (FSW) in shipbuilding. In this objective, we developed finite element based simulation methods that can help identify those conditions conducive to defect development in the welded joint. Our objective was to be able to identify processing windows that avoid conditions that promote the formation of macroscopic defects such as "wormholes." The second objective focused on advancing micromechanical models for the plastic deformation of structural alloys used in ship building. We are addressing two aspects of the mechanical behavior: the stress distribution as the metal yields under different states of stress and the yield asymmetry that develops between tension and compression following plastic deformation. As part of this objective, we developed neutron diffraction experiments with *in situ* biaxial loading that permit us to better motivate and critique the micromechanical models.

2 Defect Avoidance in Friction Stir Welding

One of the major issues associated with the successful application of friction stir welding to high strength materials like stainless steel or titanium alloys is the possible occurrence of internal defects. One type of internal defect that can be a serious problem is that of a voided zone, often called a worm hole, running parallel to the welding direction and appearing near the boundary of the stir zone. A major goal of our research is to simulate friction stir welding processes with a focus on computing conditions that lead to the formation and growth of voids associated with worm holes. Being able to reliably predict the occurrence of the voiding, allows us to search for welding conditions that minimize the risk of forming wormholes.

To simulate the formation of worm-hole type defects, we implemented a void growth model in the finite element code, ISAIAH. ISAIAH simulates viscoplastic flow and heat transfer using an Eulerian reference frame. Strain hardening and softening are included via an isotropic state variable representing the strength. The void growth model adds a second state variable to the formulation, the porosity. The porosity grows as a function of the mean stress, strength, effective strain rate, and temperature. The mathematical formulation associated with the porosity growth model is detailed in a publication stemming from the grant [1]. Below we summarize present some representative results.

Using the extended formulation, we studied the tendency for wormholes to form in stainless steel under a variety of welding conditions. Specifically, we conducted a parametric study of FSW welding of 304L stainless steel, varying the welding speeds (pin translation and rotation), the thread conditions (varying the axial traction induced by the pin), and the pin geometry (straight and fustrum). A schematic of the process is shown in Figure 1 together a typical mesh used in the simulations. Using an Eulerian formulation, the mesh remains spatially fixed and the workpiece material passes through it, entering on the left and exiting on the right (the tool position is fixed and the workpiece translates past it.) The concentric dark circles correspond to the outside radii of the pin and shoulder.

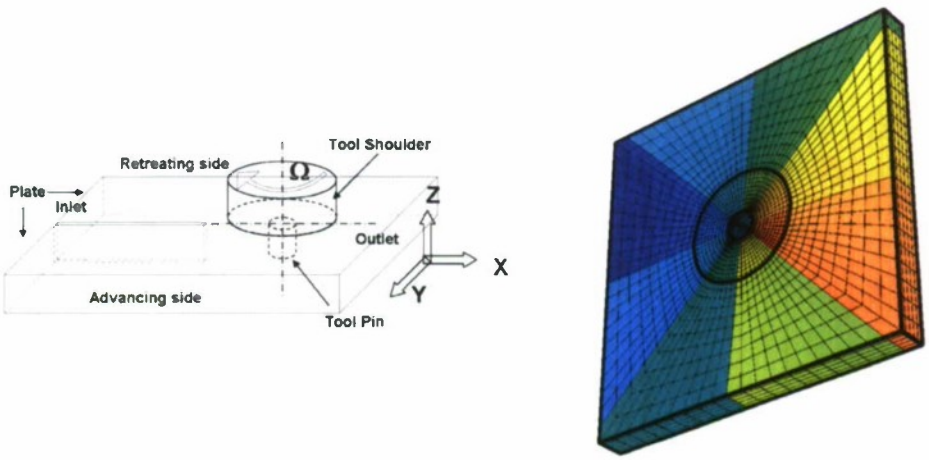

Figure 1: Left: Schematic of the FSW simulation showing the pin and workpiece. Right: Finite element mesh of the Eulerian domain. Colors are shown only to aid in visualizing the mesh construction.

ISAIAH generates a fully-coupled solutions for velocity field and temperature distributions. The action of the pin on the workpiece stirs the material in the vicinity of the pin, causing localized heating. This is evident in the temperature distribution show in in Figure 2. The highest temperatures typically are along the downstream side of the pin toward the advancing side. The temperature distributions depend on the tool translational and rotational speeds, as well as mechanical properties of the workpiece. In the case shown, the temperature rise exceeds 1000K. Once material is past the pin, conduction away from the hottest zones diffuses the temperature increase over the entire workpiece.

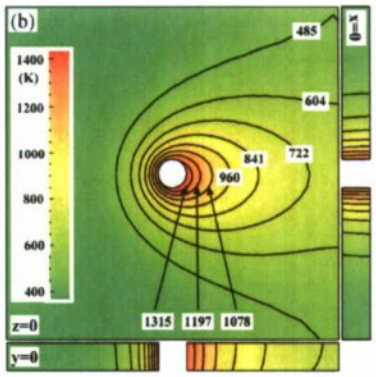

Figure 2: Temperature field for FSW of stainless steel. The figure shows temperatures on the three planes that cut through the enter of the workpiece.

The deformations associated with the stirring process also alter the material properties. This is treated in ISAIAH using a state variable that represents the material strength. This variable evolves with deformation, increasing and decreasing according to the deformation rate and the temperature. The distribution of the strength for the same welding parameters as used to compute the temperature in Figure 2 is shown in Figure 3. This particular case shows that there is a reduction in strength between the base material and the weld zone, whereas more commonly the strength in the weld zone was elevated over the base material for stainless alloys. The high temperatures computed in this case implied that the strength is also lower than the base material, and consequently the material softens as it deforms during the stirring.

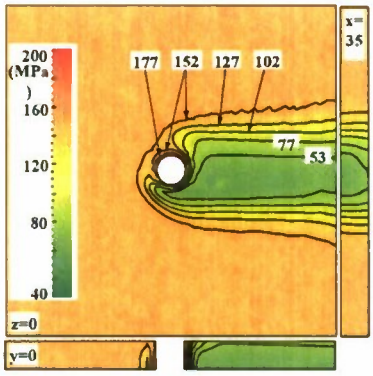

Figure 3: Strength distribution for FSW of stainless steel. The figure shows state variable for strength on the three planes that cut through the center of the workpiece.

The critical parameter in void growth is the ratio of the mean stress to the strength of the material. The mean stress is the driving force for void growth while the strength dictates the resistance the material offers against this growth. This ratio has been plotted in Figure 4 for the case illustrated in the prior two figures. Porosity will grow where this ratio is large (and positive). The highest zone of tensile mean stress to strength is behind the pin. This is where the porosity will tend to accumulate as during welding.

The growth of porosity is shown in Figure 5. The highest growth occurs on the advancing side, and toward

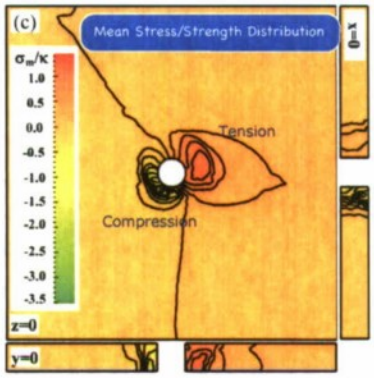

Figure 4: Ratio of the mean stress to the strength during FSW of stainless steel. The figure shows the ratio on the three planes that cut through the enter of the workpiece.

the bottom surface. The presence of the tool shoulder induces compressive mean stress on the top surface, which suppresses the porosity evolution. Overall, the values of porosity remain low in this case and a wormhole would not be expected to form.

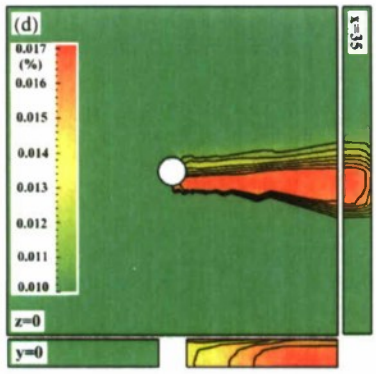

Figure 5: Porosity distribution during FSW of stainless steel. The figure shows the porosity on the three planes that cut through the enter of the workpiece.

The example shown above had a straight, threadless pin. This is not a severe case from the perspective of generating porosity. Threading of the pin tends to promote flow in the through-thickness direction and with it that flow some zones of higher tensile mean stress. This is demonstrated in the next two plots (Figures 6 and 7) that show the porosity predicted for welding with a fustrum shaped pin, in one case without thread and the other with threads. The threadless pin case shows porosity levels similar to that of the straight, threadless pin with values below a level where a wormhole might be expected. With the introduction of the threads, the porosity levels are much higher. The location of the peak values – on the advancing side and slightly elevated from the bottom surface – are consistent with observed wormholes in similar systems.

Overall, from the parametric study, the trends that emerged were: porosity accumulates more readily on the advancing side of the weld near the pin region; the pin threads have the most substantial effect on the magnitude of the porosity; porosity occurs more readily near the bottom surface with straight pins and toward the centerplane with fustrum pins; fustrum pins generate more heat than straight pins, making for hotter welding conditions; and, the welding speeds strongly influence the temperature, but have little impact on the porosity.

The effort devoted to modeling the onset of wormhole defects was successful in demonstrating the viability of this approach. We implemented a model for porosity growth and used it to examine the sensitivity of defect formation to various welding parameters. Ongoing work will include some refinements of this capability and further comparison to welding experiments. Under this objective of the grant, we also devoted time to completing our examination of the strain hardening and texture evolution in 304L stainless steel (initiated under the preceding grant.) This consisted of

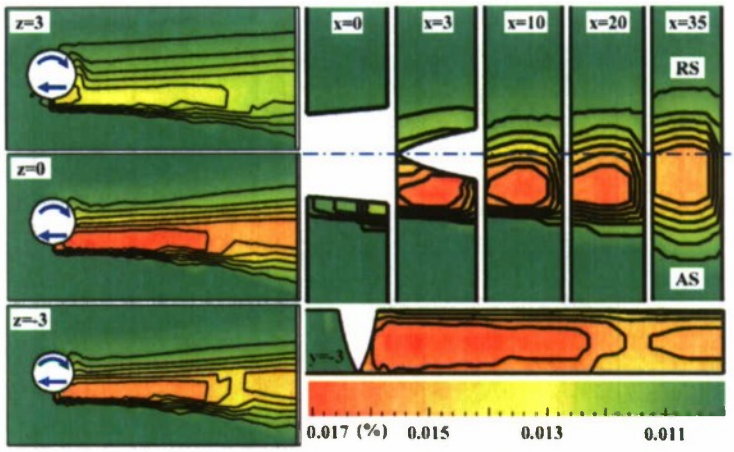

Figure 6: Porosity distribution around the pin for a threadless pin.

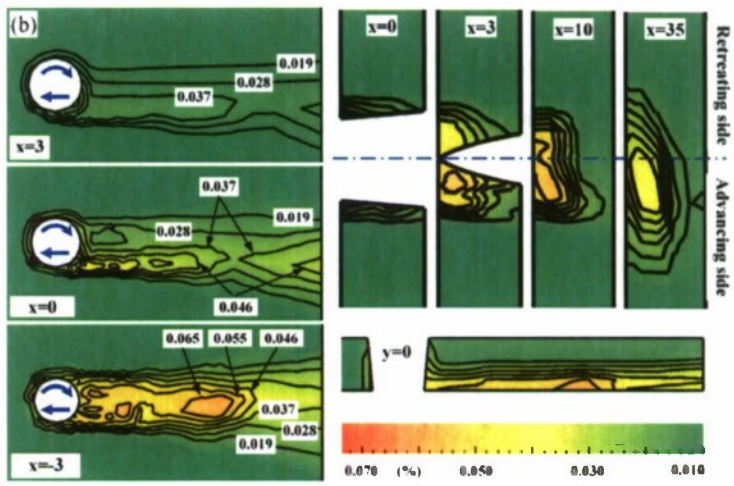

Figure 7: Porosity distribution around the pin for a threaded pin.

publishing two articles, one focussed on the strength distribution over the stir and heat affected zones [2] and the other to a comparison of measured and computed texture distributions [3].

In addition to the specific goal of modeling the occurrence of wormholes, we also maintained a goal of being able to compute the thermomechanical histories for experimental efforts being conducted by other researchers working under ONR support. In particular, we conducting simulations to predict the thermomechanical behavior in welding of titanium alloys. The simulation parameters are established by experiments coordinated by NSWCC (data courtesy of Jennifer Nguyen-Wolk). We determined the flow parameters (constitutive parameters for the viscoplasticity model) for Ti-6Al-4V that will be employed as representative of this class of titanium alloys and conducted a number of simulations corresponding to NSWCC experiments.

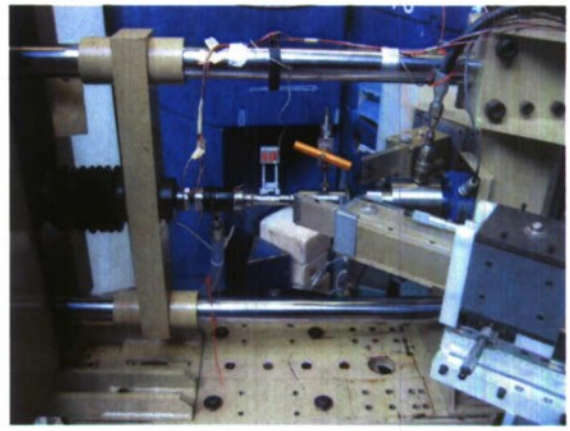

Figure 8: Biaxial loading experiments: (left) drawing of the biaxial sample and fixturing; (right) photograph of the biaxial sample mounted in the *in situ* load frame.

3 Finite Element Simulation of High Fidelity Polycrystals

Finite element modeling of metallic alloys, particularly polycrystalline systems, has provided considerable insight in the behaviors of these materials. As outlined in a summary article (chapter) we wrote for the new version of the ASM Metals Handbook - Volume 22 [4], this modeling helps to better understand material behavior in applications ranging from fabrication processes (like rolling, forging and welding) to evaluating the performance of materials under design loading (such as determining how materials respond under different loading modes). As part of this project, we completed several thrusts related to developing better modeling capabilities associated with finite element simulations of polycrystalline materials. One thrust included the development of experimental capability to load material under different levels of stress biaxiality while measuring lattice strains by neutron diffraction. The data from these experiments has provided a rich basis for critiquing and refining the finite element simulations. A second thrust involved expanding the formulation to include the effects of incomplete slip within crystals. Incomplete slip is a source of excess dislocations that account for the formation of dislocation structures. These structures impact the mechanical performance by modifying the stress state locally. We also worked on visualization capabilities with the intent of being able to merge various aspects of the solution, including the evolving microstructural distributions and the changing stress field. Here, we sought to develop the capability to improve our interpretation of the results by better visualizing dependencies or correlations that emerge from a simulation. Finally, we completed work that was initiated several years ago under ONR funding on the stability of texture components under large strain deformations [5].

3.1 Biaxial loading investigation

Samples subjected to uniaxial loading provide information related only to one simple, macroscopic, deformation mode. Obviously, other simple modes are important as well, not to mention more complex situations with variable loading paths. Data for these cases are crucial for developing a comprehensive understanding of how stress and deformation are distributed over loaded polycrystalline materials. Performing multiaxial loading experiments while conducting diffraction measurements is far from trivial, however, and examples of such are few. As part of this project, we completed the design of an experimental set-up that enables the *in situ* measurement of lattice strains by neutron diffraction in samples subjected to specified levels of biaxial loading [6], as shown in Figure 8. The set-up achieves a biaxial stress state using tubular specimens that are simultaneously pulled in tension and pressurized internally and facilitates controlling the level of biaxiality from uniaxial tension to balanced biaxial tension. An advantage of the design is that the level of biaxiality can be altered without changing the orientation of the principal directions of the stress with respect to the material's microstructure. A disadvantage of the design is that the stress is not uniform over the gauge volume: the circumferential component of the stress varies through the tube wall and the radial component of the stress, although generally small in comparison to the other stress components, is not identically zero anywhere except at the outer diameter of the tube. This concern was addressed through examination of the variation of the stress within the diffraction volume. Figure 9 shows the loading programs for achieving different levels of stress biaxiality

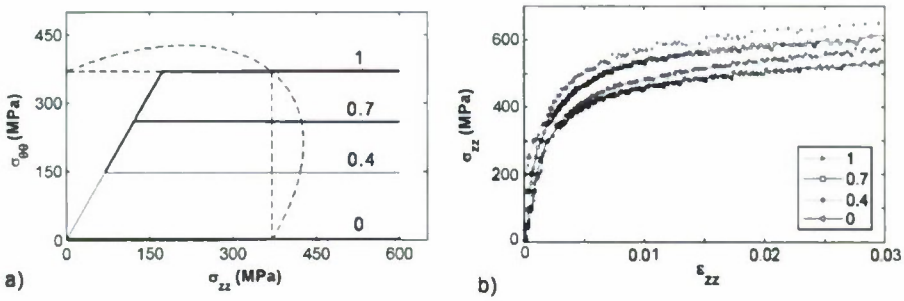

Figure 9: Biaxial loading experiments: (a) loading program for pressure and axial load sequence to produce axial and hoop stress components with different biaxiality ratios; (b) measured macroscopic axial stress-strain responses for four levels of stress biaxiality.

at approximately the onset of plastic yielding. The measured axial stress-axial strain curves are also provided in this figure. It can be seen that increasing the hoop component of stress via higher pressure results in higher axial stress compoent throughout the loading program.

We measured the measured responses of a stainless alloy under varying levels of stress biaxiality. The levels of single crystal elastic and plastic anisotropics have a direct bearing on the differences between the average lattice strains associated with observed crystallographic fihers (namely, those corresponding to the combinations of crystallographic planes and scattering vectors measured in the experiments). Interesting trends are apparent in these differences as a function of the stress biaxiality, as plotted in Figure 10 and condensed to a single level of axial stress in Figure 11. By considering the orientational dependence of the lattice strain under prescribed stress, assuming as a first approximation that the crystal stresses equal the nominal stress, the trends were explained in part in terms of the relative contributions of the deviatoric and mean portions of the stress to the lattice strain. The theoretical values for lattice strain, assuming the nominal stress in each crystal, is shown in Figure 12 for several levels of elastic anisotropy. An intermediate value of anisotropy leads to lattice strain values that are in reasonable agreement with experiment. However, some contradictions arise, which were investigate further in terms of roles of plasticity and spatial heterogeneity of the deformation using our finite element models with highly resolved crystals.

Using the finite element formulation, we replicated the loading on a sample of material corresponding to the diffraction volume of the experiment. The finite element mesh is built to provide a virtual polycrystal by arranging elements into grains. Figure 13 depicts a virtual polycrystal that was deformed under balanced biaxial tension, with the wireframe showing the original sample dimensions. Lattice strains were extracted from the simulation results that correspond to those measured. A comparison between the finite element simulations and the experimental measurements is provided in Figure 14, along with the corresponding predictions from the theoretical, uniform stress computations. Overall, the finite element results capture the experimental trend much better than is possible assuming a uniform state of stress. The stress varies spatially because the crystal anisotropy effectively gives directionality to the moduli. The finite element solution captures this heterogeneity by providing a solution that simultaneously satisfies equilibrium, kinematics, and the constitutive equations, rather than imposing the over-simplified assumption of uniform stress. In doing so, the finite element solution is exposing the physical nature of the grain interactions. Additional comparisons were made to explore the role of biaxiality for the stress on the deformation when loading proceeds well into the elastoplastic regime. These results are quite encouraging and will be submitted for publication.

In addition to the tests performed on stainless, we also conducted experiments on a titanium alloy (Ti 5111). An initial round of experiments were completed, loading the samples to the point of failure. Photographs are shown in Figure 15 for samples loaded at two different levels of stress biaxiality. Note that under balanced biaxial stress the sample developed a fracture running in the axial direction. At lower biaxiality, the fracture ran circumferentially around the sample. We were not able to complete these experiments as the neutron source was shut down following a leak in the reactor vessel at Chalk River. It remains our intent to finish the experiments when the facility returns to operation (Fall, 2010).

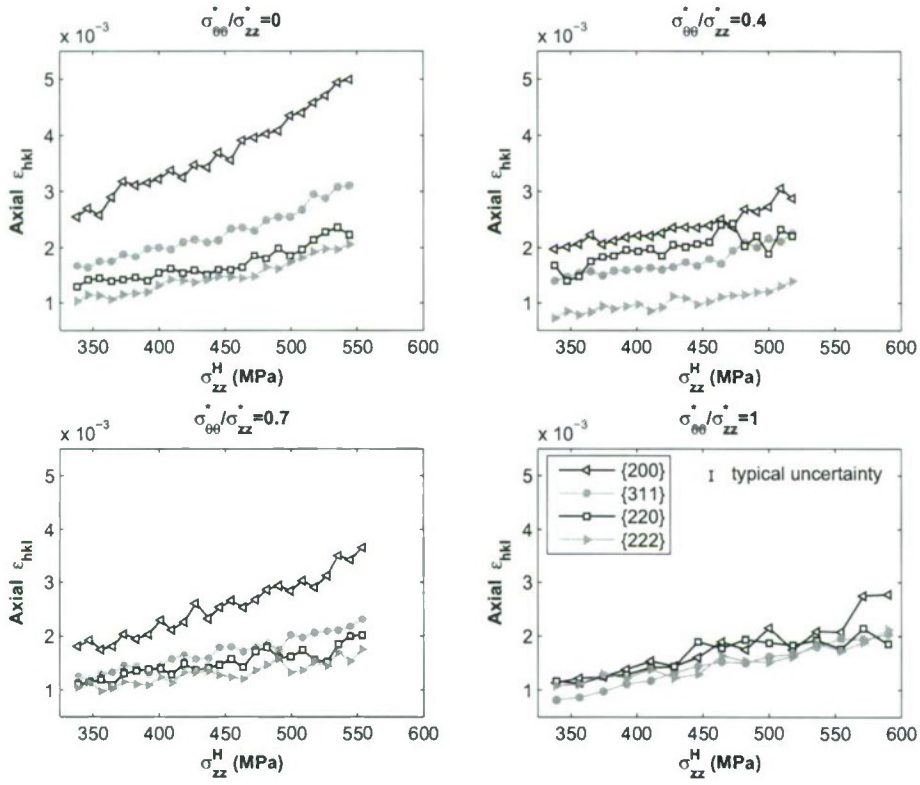

Figure 10: Biaxial loading experiments: measured lattice strains under load for four levels of stress biaxiality grouped according to (*hkl*).

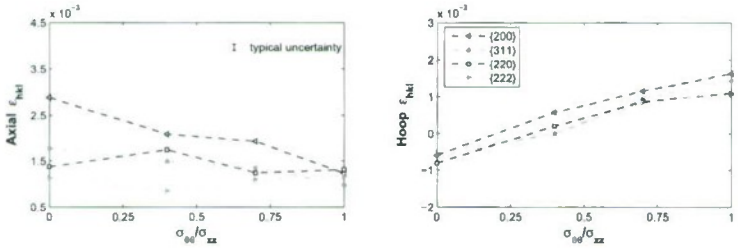

Figure 11: Biaxial loading experiments: measured axial and hoop lattice strains grouped by (*hkl*) taken from Figure 10 at an axial stress of 370MPa for various levels of stress biaxiality.

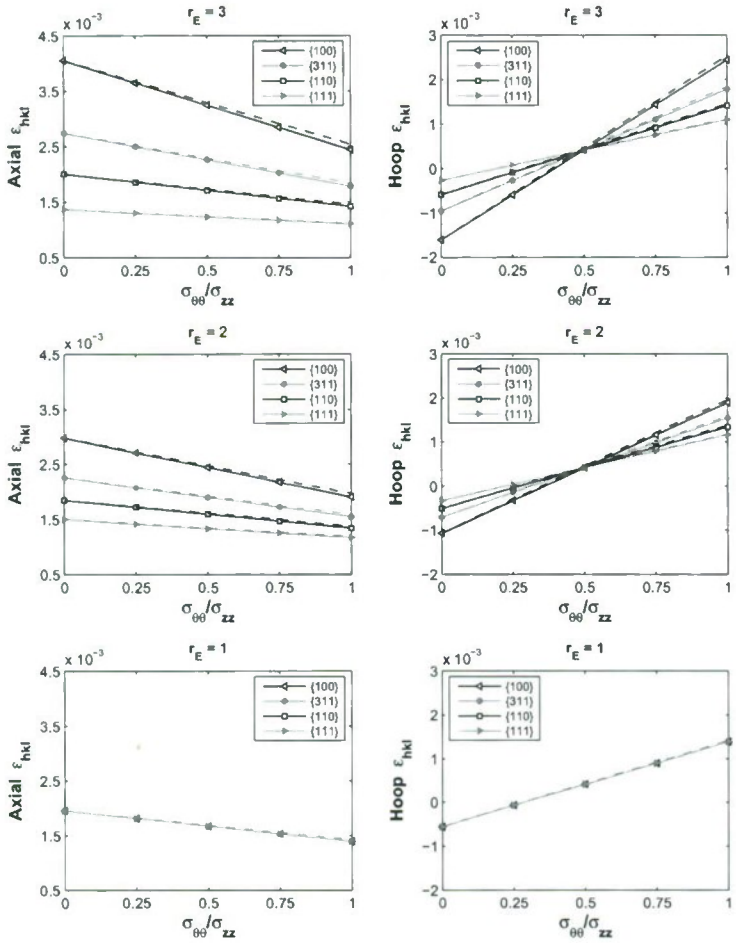

Figure 12: Estimates of the lattices strains assuming that same stress is active for all crystals irrespective of the lattice orientation.

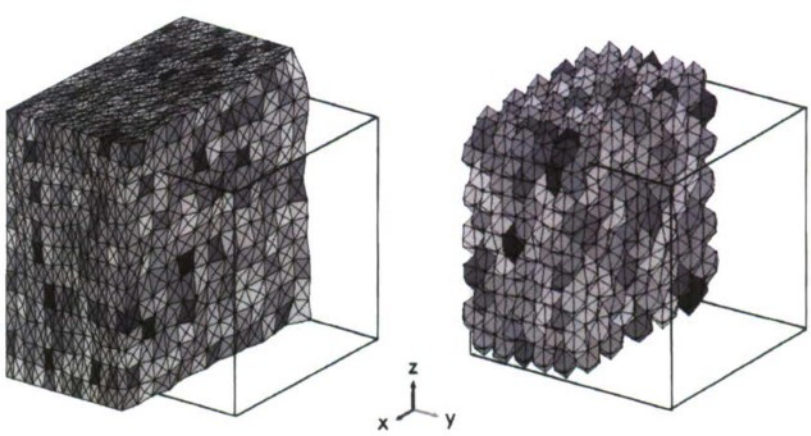

Figure 13: Biaxial loading experiments: virtual polycrystal used to simulate the mechanical response of the material within the diffraction volume of the biaxial tests.

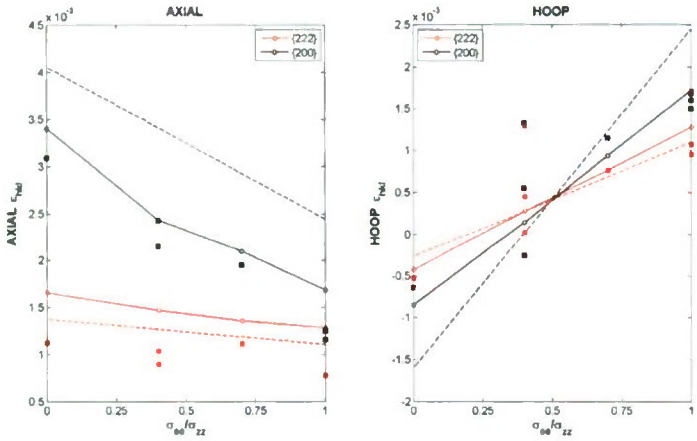

Figure 14: Biaxial loading experiments: comparison of model results with experiment for the lattice strains at an axial stress of 370MPa for various levels of stress biaxiality. Note that the pair of experimental data points near 1.5×10^{-3} for the hoop strain component at stress biaxiality of 0.4 are considered to be in error due to difficulties encountered with controlling the loading in that particular experiment. Experimental data are shown as points (squares), finite element simulations are lines with circles, and the uniform stress computations are lines without symbols.

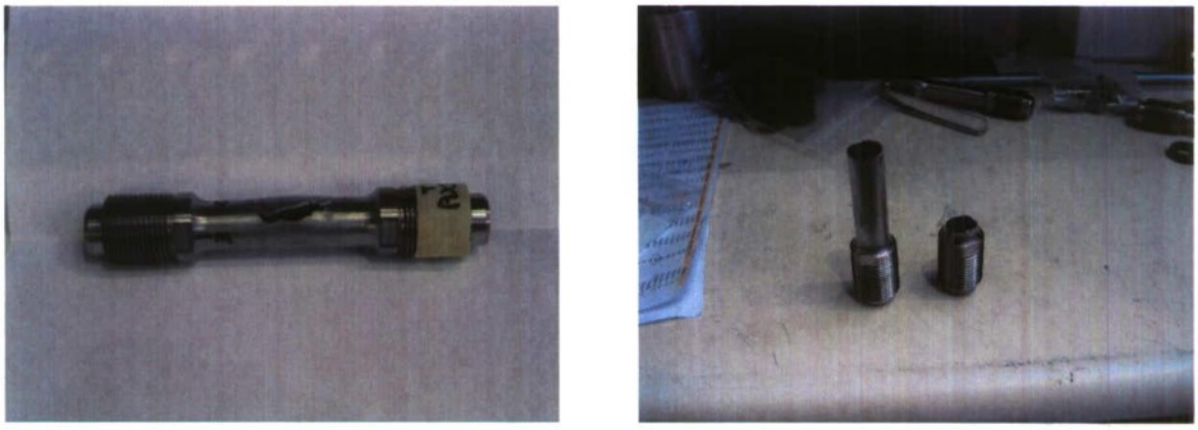

Figure 15: Biaxial loading experiments: (left) failed titanium sample under loading with stress biaxiality of 1.0; (right) failed titanium sample under loading with stress biaxiality of 0.4.

3.2 Yield asymmetries following plastic deformation

Deformation typically is not spatially uniform at the scale of individual crystals within a polycrystalline solid. The nonuniformity of strain can have important consequences for the microstructural state of a metal as well as its derivative properties. We investigated using an extension to the standard crystal elastoplastic framework that embodies varying slip over the volume of a crystal [7, 8, 9]. Gradients in the slip have two potential effects: elevated rate of hardening of the slip systems and the introduction of long-range elastic strains from residual dislocation content. As part of this study, we examined behavior of single grain systems in which gradients in straining are introduced by means of the boundary conditions, in this case bending.

Bending deformation naturally includes a variation in the deformation ranging from a high tension or compression deformation on the outer surface to zero deformation at the neutral axis. The behavior of the extended model was investigated by simulating the bending of a thin foil of single crystal aluminum with a thickness of $t = 25\mu$m. A comparison of the yielding behavior with simulations of foils of other thickness show that both isotropic and kinematic type hardening behavior results from the slip gradient effects. These observed behaviors are connected to the increase in dislocations that appear due to slip gradients and the stress field that results from the build up of these dislocations.

The specimen, shown in Figure 16, is a single FCC crystal and the crystal axes are aligned with the specimen axes. A velocity is applied to the lower right edge of the specimen, inducing a bending moment and a small amount of compression in the gage section. The gage section is 0.5 mm long, 0.25 mm wide and $t = 25\mu$m thick (simulations using 50, and 100μm thick samples are reported in [7]). The slip rate gradient boundary condition was specified to enforce zero flux of geometrically necessary dislocations across the surface. A mesh of the sample also is shown in Figure 16. This mesh was chosen such that the element scale is significantly larger than the scale chosen for the length parameter in the long range stress. If this were not the case, the physical interpretation of the long range formulation would conflict with the numerical model represented by the mesh. For results presented here, the length parameter for the long range strain term and the gradient hardness coefficent (for the elevated hardening term) are $a = 1\mu$m and $\beta = 1 \times 10^{-6}\sqrt{m}$, respectively. The length parameter was selected to be below a typical crystal size but larger than the scale relevant to individual dislocations. This range of length scales then would capture the *average* effects of sub-crystal behavior such as a distribution of dislocation pile-ups. The gradient hardness coefficient was chosen to provide demonstrative simulation results.

Shown in Figure 17 are contours of the evolving Voce hardness at the end of each bending and straightening cycle. The value contoured is the element average Voce hardness calculated by volume averaging the values at each element's integration points. During each subsequent cycle of deformation, the relative pattern does not change appreciably, however the magnitude continues to evolve. The relative hardness magnitude indicates more plastic deformation near the front and back edges of the foil. Simulations using other sets of parameters that include long range and/or gradient hardness effects show very similar relative patterns with the hardness generally varying less than 5% from the results show in Figure 17. The gradient hardness at the end of each bending and straightening cycle is shown in Figure 18. These results show that the gradient hardness is on the order of 10% of the Voce hardness. Increasing the gradient hardness coefficent to $\beta = 2 \times 10^{-6}\sqrt{m}$ results in a gradient hardenss about twice that shown in Figure 18. The gradient hardness pattern shows a large gradient effect at the ends of the foil strip near the tapered sections. The patterns in the foil away from the ends have little correlation amongst the models or to the Voce hardness patterns. There are notable changes between the fully bent and fully straightened deformations that indicate a somewhat uniform gradient hardness along the width direction at fully bent and a relative reduction in gradient hardness near the edges at fully straightened. The evolution of the pattern at fully straightened for each of the simulations indicate less variation in the gradient hardness with each subsequent straightening cycle. Figure 19 shows the von Mises effective long range strain. In general, these figures show that the bent specimen has elevated long range strain near the center of the gage section and for the straightened specimen the pattern shifts to elevated magnitude near the edges of the gage section. The patterns continue to evolve throughout the three cycles but generally maintain these regions of relative magnitude. For the same long range strain length parameter, $a = 1.0\mu$m, but different values of gradient hardness parameter, the results indicate the gradient hardness has a noticeable effect on the long range strain. Additionally, changing the long range strain length parameter to $a = 0.9\mu$m and $a = 1.1\mu$m results in a change in the magnitude of the effective long range strain in proportion to the change in length parameter and a slight change in the pattern of effective long range strain (see [7]).

Shown in Figure 20 is the scaled moment (M/bh^2) versus the strain on the top surface of the foil for six different simulations using different long range strain length parameters and gradient hardness coefficients. The scaled moment is thickness-independent measure of bending stress and is the applied moment M scaled by the width times height

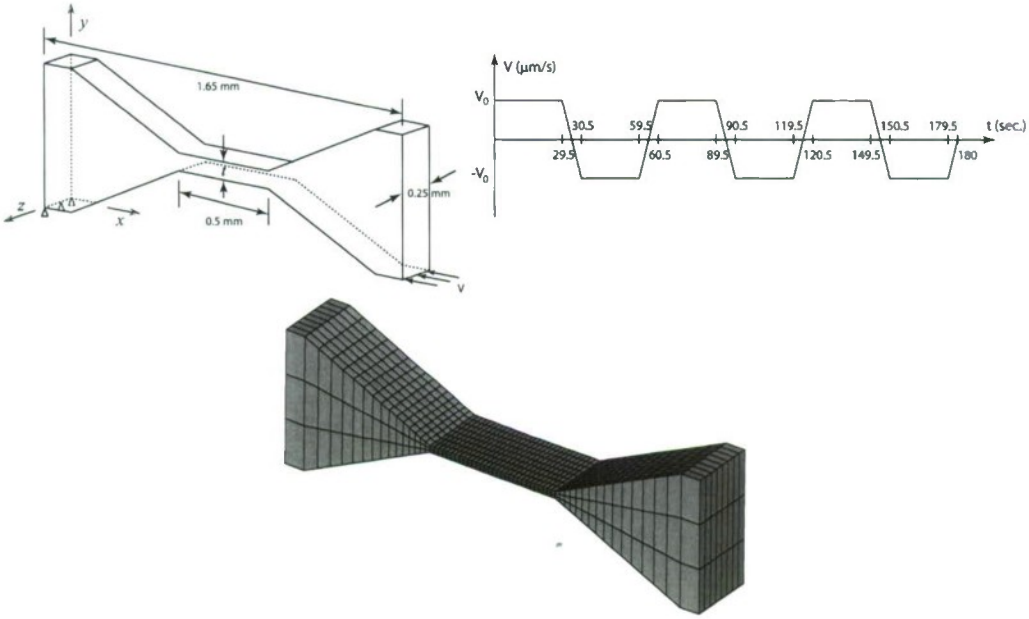

Figure 16: Single crystal foil bending sample. A constant velocity, V_0, is applied to the loaded edge for approximately 30 s, bending the specimen so that the top surface of the gage section strains to 0.04. The velocity is then reversed to straighten the specimen back to (nearly) the original position. This loading cycle is performed three times. The mesh contains 1,488 quadratic 20 node hexahedral elements and a total of 8,217 nodes.

squared. The plot shows overlaid results for each individual bending/straightening cycle.

In the first cycle an initial yield is the scaled moment when the strain on the top surface is 0.001 and the yield at the start of straightening is the scaled moment when the strain on the top surface is 0.038. The unloading scaled moment is the maximum shown in the figure. The initial, primarily elastic, behavior of each of the six simulations is very similar. However, during the initial stages of yielding, differences in the results become apparent. The initial yield point for the model without long range and gradient hardness effects is the lowest of the six simulations at 2.73 MPa while the highest initial yield is for the model with a size parameter of $a = 1\mu$m and a gradient hardness coefficient of $\beta = 2 \times 10^{-6}\sqrt{m}$. Of the models that include long range and/or gradient hardness effects, the lowest initial yield is for the model with zero gradient hardness coefficient and the highest corresponds to the highest gradient hardness coefficient. For the three simulations with a gradient hardness coefficient of $\beta = 1 \times 10^{-6}\sqrt{m}$ there is little difference in the behavior near the initial yield point. However, the models quickly distinguish themselves.

The significant influence of the long range and gradient hardness on the material behavior is readily apparent. The model without these effects requires a scaled moment of 4.29 MPa at maximum curvature while the models including these effects require, on average, 8.5 MPa. The relative differences between the models with long range and gradient hardness effects developed during initial yield continues through the beginning of unloading. In other words, the model with the highest gradient hardness coefficient shows the highest unloading scaled moment and the model with zero gradient hardness shows the lowest unloading scaled moment. After unloading, the yield behavior at the start of the straightening (*i.e.*, reverse yield) shows a shift in the yield compared to the model without long range and gradient hardness effects. The reverse yield for the model without long range or gradient hardness effects is nearly the same magnitude as the scaled moment at unloading while the models with these effects show a shift in yield of approximately 4 MPa. Upon reverse yielding each of the three models with $\beta = 1 \times 10^{-6}\sqrt{m}$ show similar behavior, with the distance between the unloading scaled moment and the reverse yield value being nearly identical. The model with $a = 1.1\mu$m has a reverse yield that is notably higher than these three while the reverse yield for the model with $a = 0.9\mu$m is notably lower. These results indicate that the gradient hardness coefficient causes an isotropic type hardening effect while the long range strain causes a kinematic type hardening effect. This effect can be seen in the difference between the unloading scaled moment and the reverse yielding scaled moment.

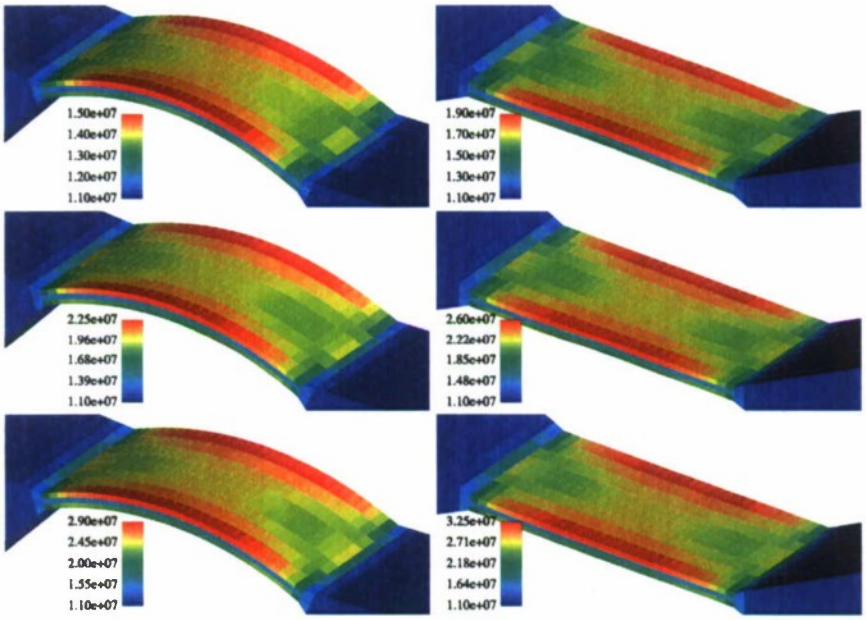

Figure 17: Contours of the Voce hardness at points of maximum and minimum flexures over the three bending cycles. Distributions are shown for values of the length parameter and gradient hardness coefficent of $a = 1\mu$m and $\beta = 1 \times 10^{-6}\sqrt{m}$, respectively. Units are Pa.

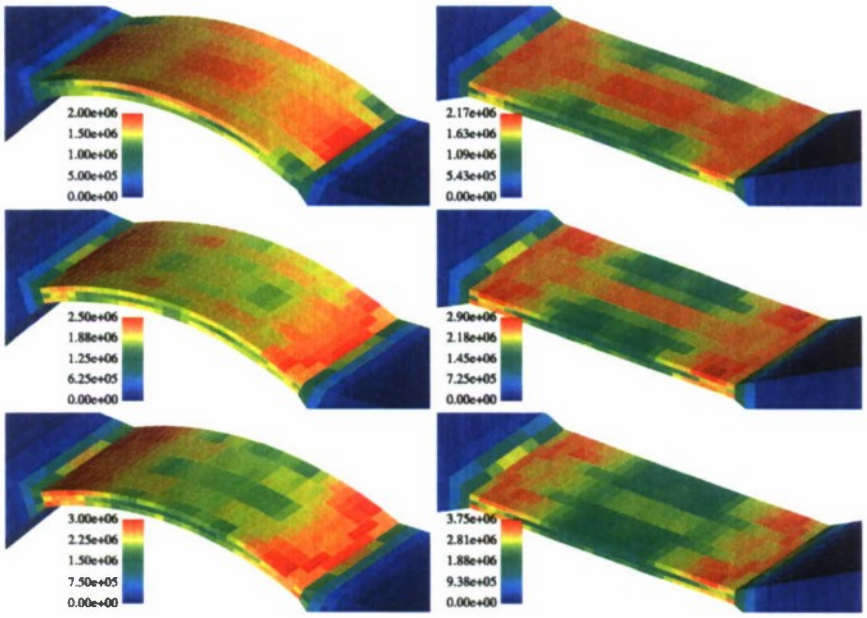

Figure 18: Contours of the gradient hardness at points of maximum and minimum flexures over the three bending cycles. Distributions are shown for values of the length parameter and gradient hardness coefficent of $a = 1\mu$m and $\beta = 1 \times 10^{-6}\sqrt{m}$, respectively. Units are Pa..

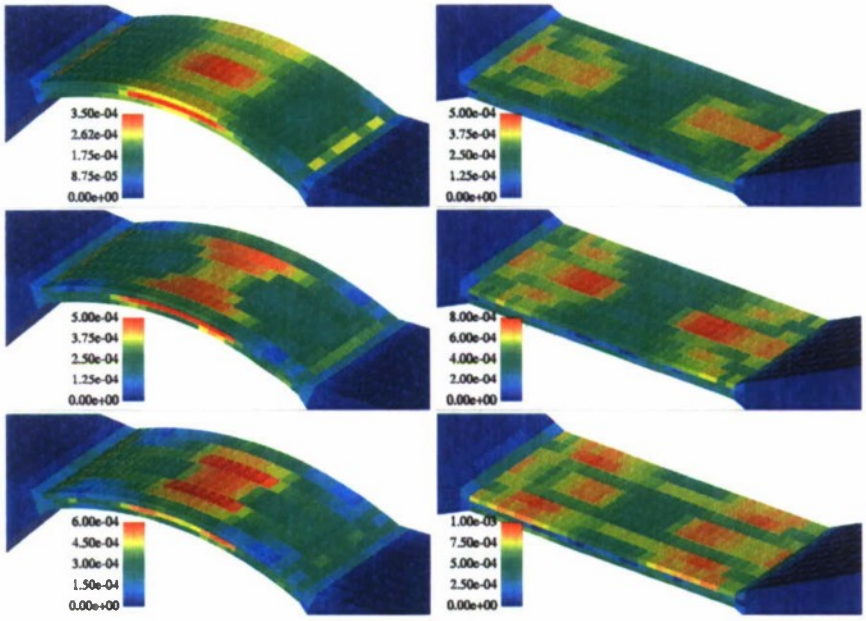

Figure 19: Contours of the effective values of the long range strain at points of maximum and minimum flexures over the three bending cycles. Distributions are shown for values of the length parameter and gradient hardness coefficent of $a = 1\mu$m and $\beta = 1 \times 10^{-6}\sqrt{m}$, respectively. Dimensionless scales.

3.3 Visualization capabilities

Simulations generate large data sets which become difficult to interpret just due to their size. In simulating the deformation of polycrystals, the data sets include fields of stress and strain tensors and for descriptors used to quantify the microstructural state (such as vectors for the lattice orientations and sets of scalars for the slip system strengths). Visualization of the data is essential in understanding their influence on the mechanical response. Further, detecting and rationalizing apparent correlations between variables is an intended outcome of simulation, but is very difficult to achieve without the aid of effective visualization tools. This is especially true for connecting the mechanical response with the microstructural state. As part of this project we have developed visualization capability that facilitates discovery and quantification of connections between attributes of the local microstructure and the mechanical response under load. This capability is built on the coupling of two existing programs: openDX for visualization and MatLab for postprocessing of simulation data.

Our program, called DxPx (short for DX polycrystal viewer), is designed for selective visualization of large data sets. For a very large data set, it is rarely necessary or even feasible to view every data point in complete detail. It is much more useful to select certain subsets of particular interest and view those in detail. To illustrate, we show some images derived from a simulation of titanium under uniaxial tension, with grains built using regular rhombic dodecahedra. Our first level of selection is done by choosing a point on the time-load (analagous to stress-strain) curve (see Figure 21). Data frames are available at several locations on the curve; the red dot shows the selected frame. When the frame is selected, DxPx makes a call to matlab requesting more information about the data available in that particular frame. The user selects the (1,1) component of stress to use for building a histogram of grain data values. The histogram is shown in Figure 22. Now, each bar of the histogram can be selected set the list of grains to view. A sample view is shown in Figure 22. The data shown are values of (1, 1) stress, but other data could be shown. Many other options are available in DxPx, but the essential idea is to use data statistics to select interesting subsets of data for detailed visualization.

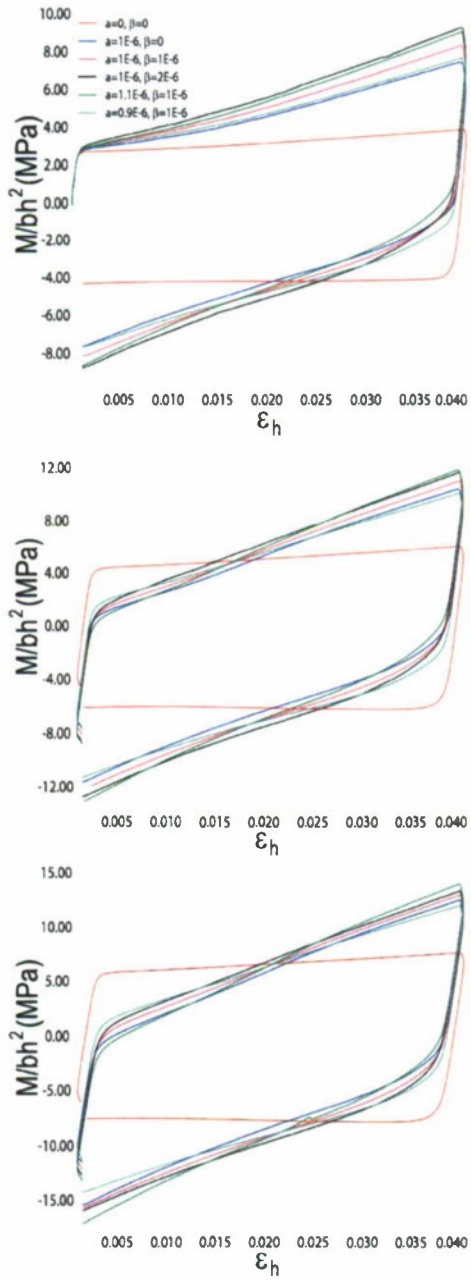

Figure 20: Moment versus maximum strain for a 25μm thick gage section: overlaid results for the six simulations comparing scaled moment versus top surface strain. The plots show, from left to right, cycles 1, 2 and 3, respectively.

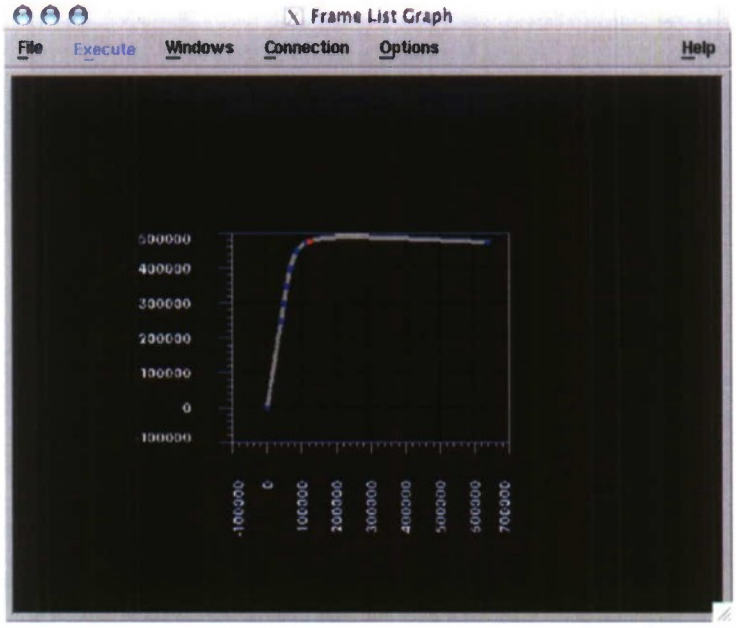

Figure 21: Load curve showing available frames in blue and selected frame in red. Frames contain data from the simulation at a particular point in the simulation. The data include geometry, stress and strain distributions, and microstructure fields (lattice orientations and slip system hardnesses).

4 Summary

This report provides the technical summary and a few representative results of the research conducted at Cornell University under the support from the Office of Naval Research under Grant N00014-06-1-0241. The research had two primary objectives. The first objective focused on developing finite element based simulation methods that can help identify those conditions conducive to defect development in the welded joint. We implemented the capability to identify processing windows that avoid conditions that promote the formation of macroscopic defects known as wormholes in a finite element formulation for coupled viscoplastic flow and heat transfer. Using the simulation capability we computed the sensitivity of defect formation to a number of variables associated with friction stir welding, including pin and pin thread geometries. The second objective focused on advancing micromechanical models for the plastic deformation of structural alloys used in ship building. We are addressing two aspects of the mechanical behavior: the stress distribution as the metal yields under different states of stress and the yield asymmetry that develops between tension and compression following plastic deformation. As part of this objective, we developed neutron diffraction experiments with *in situ* biaxial loading that permit us to better motivate and critique the micromechanical models. Finally, we developed a powerful new capability for examining the simulation results that permits a researcher to re-process simulation data on-the-fly to facilitate exploring trends that emerge by superimposing structure and performance data. A number of archival publications were completed under this funding, which are listed in the References section of this report.

References

[1] Y. He, P. R. Dawson, and D. E. Boyce. Modeling damage evolution during friction stir welding of stainless steel. *Journal of Engineering Materials and Technology*, 130:021006–1 – 021006–10, 2008.

[2] J.-H. Cho, D. E. Boyce, and P. R. Dawson. Modeling strain hardening during friction stir welding of stainless steel. *Modeling and Simulation in Materials Science and Engineering*, 15:486–489, 2007.

Figure 22: Histogram of the (1,1) component of the Cauchy stress tensor averaged over elements within a grain at the selected frame. One can select on an individual histogram bar to view on the finite element mesh all the grains in that range, as shown in Figure 23.

[3] J.-H. Cho, D. E. Boyce, and P. R. Dawson. Modeling texture evolution during friction stir welding of stainless steel with comparison to experiments. *Journal of Engineering Materials and Technology*, 130:01007–1 – 011007–12, 2008.

[4] P. R. Dawson and D. E. Boyce. Crystal-scale simulations using finite element formulations. In D. U. Furrer and S. L. Semiatin, editors, *ASM Handbook of Metals*, volume 22A – Fundamentals of Modeling of Metals Processing, pages 246–259. American Society of Materials, 2009.

[5] A. Kumar and P. R. Dawson. Dynamics of texture evolution in face-centered cubic polycrystals. *Journal of the Mechanics and Physics of Solids*, 57:422–445, 2009.

[6] T. Marin, P. R. Dawson, M. A. Gharghouri, and R. B. Rogge. Diffraction measurements of elastic strains in stainless steel subjected to *in situ* biaxial loading. *Acta Materialia*, 56:4183–4199, 2008.

[7] J. M. Gerken and P. R. Dawson. Bending of a single thin foil of material with slip gradient effects. *Modeling and Simulation in Materials Science and Engineering*, 15:799–822, 2007.

[8] J. M. Gerken and P. R. Dawson. A crystal plasticity model the incorporates stresses and strains due to slip gradients. *Journal of the Mechanics and Physics of Solids*, 56:1651–1672, 2008.

[9] J. M. Gerken and P. R. Dawson. A finite element formulation to solve a non-local constitutive model with stresses and strains due to slip gradients. *Computer Methods in Applied Mechanics and Engineering*, 197:1343–1361, 2008.

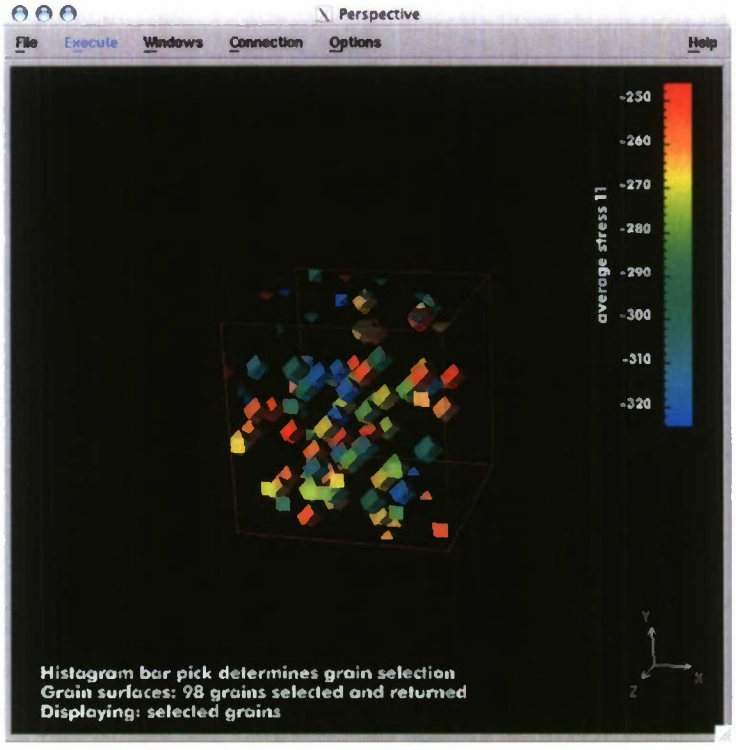

Figure 23: Crystals showing the values of the (1,1) component of the Cauchy stress within one bar of the histogram shown in Figure 22. Note that the range of the scale corresponds to one bin of the histogram. Displaying other data fields is easily done; for instance one might want to examine the orientations of the crystals within this bar of the histogram.